LITHOS 404–405 (2021) 106483

Contents lists available at ScienceDirect

LITHOS

journal homepage: www.elsevier.com/locate/lithos

Research Article

EoS of mantle minerals coupled with composition and thermal state of the lithosphere: Inferring the density structure of peridotitic systems

Luca Faccincani [a,*], Barbara Faccini [a], Federico Casetta [a,b], Maurizio Mazzucchelli [c], Fabrizio Nestola [d], Massimo Coltorti [a,e]

[a] Department of Physics and Earth Sciences, University of Ferrara, Via Saragat 1, 44121 Ferrara, Italy
[b] Department of Lithospheric Research, University of Vienna, Althanstraße 14, 1090 Vienna, Austria
[c] Department of Chemical and Geological Sciences, University of Modena and Reggio Emilia, Via Campi 103, 41125 Modena, Italy
[d] Department of Geosciences, University of Padua, Via Gradenigo 6, 35131 Padua, Italy
[e] Istituto Nazionale di Geofisica e Vulcanologia (INGV) Sezione di Palermo, Via Ugo la Malfa 153, 90146 Palermo, Italy

ARTICLE INFO

Keywords:
Equations of State
Mantle minerals
Upper mantle density structure
Fertile and depleted peridotites
Cold-hot geotherms

aaa

ABSTRACT

Unravelling the physical state and properties of mantle rocks is crucial for understanding both plate tectonics, seismic activity, and volcanism. In this context, the knowledge of accurate elastic parameters of constituent mineral phases, and their variations with pressure (P) and temperature (T), is an essential requirement, that coupled with the thermal state of the lithosphere can provide a better understanding of its petrophysics and thermochemical structure.

In this paper, we present an assessment of the thermoelastic parameters [in the form of P–V–T–K Equations of State (EoS)] of orthopyroxene, clinopyroxene, spinel and garnet based on X-Ray diffraction data and direct elastic measurements available in literature. The newly developed EoS are appropriate to describe the elastic behaviour of these phases under the most relevant P–T conditions and bulk compositions of the Earth's mantle. In combination with the published EoS for mantle olivine and magnesiochromite, these EoS are suitable to calculate the physical properties of mantle peridotites and their variation with P and T.

Thanks to these EoS, we can evaluate how the variations in bulk composition and thermal regimes affect the density structure of the lithospheric mantle. Accordingly, the density structure of fertile and depleted peridotitic systems was calculated along the 35, 45 and 60 mWm^{-2} geothermal gradients at P comprised between 1 and 8 GPa. Under very cold geothermal gradients, the density of both fertile and depleted peridotitic systems progressively increases with depth, whereas under relatively hot conditions a first downwards decrease from 1 to ca 3 GPa is observed, followed by an increase downward. In mantle sections characterized by intermediate geotherms (45 mWm^{-2}), the behaviour of the two systems differs up to ca 4 GPa, as the density of the depleted system remains nearly constant down to this depth whereas it moderately increases in the fertile system.

The results of our simplified parameterisation, in agreement with classical thermodynamic modelling, indicate that the density structure of the lithospheric mantle is predominantly controlled by the P – T gradient variations, with some compositional control mostly arising at cold-intermediate thermal conditions. Integrated by geophysical and thermodynamic modelling, the newly developed and selected EoS could provide an alternative strategy to infer the elastic properties of mineral phases and peridotite rocks, under the most relevant P–T conditions and compositions of the Earth's mantle, without requiring sets of end-member properties and solution models.

1. Introduction

Understanding the density structure of the upper mantle is critical to our comprehension of the tectonic and magmatic evolution of the lithosphere (e.g., Braun, 2010; Capitanio et al., 2007; Simon and Podladchikov, 2008; Thybo and Artemieva, 2013) and crucial to address complex geodynamic phaenomena (e.g., mantle convection, plume upwelling, slab subduction, crustal movements). The density of the upper

* Corresponding author.
E-mail address: luca.faccincani@unife.it (L. Faccincani).

https://doi.org/10.1016/j.lithos.2021.106483
Received 17 March 2021; Received in revised form 16 September 2021; Accepted 16 September 2021
Available online 22 September 2021

mantle ultimately depends on both its thermal and compositional structure, which can be derived from petrological-geochemical studies on exhumed mantle samples, i.e., xenoliths and tectonically exposed mantle sections, and from the interpretation of seismic data (and in general of geophysical observables, e.g., gravity anomalies, surface heat flow, etc.).

Thermobarometric, petrochemical and isotopic studies of xenoliths and exposed mantle sections can help in unveiling the compositional and thermal structure of their source mantle at the time of the eruption or emplacement (e.g., Coltorti et al., 2021; Mazzucchelli et al., 2009; Melchiorre et al., 2020; Pearson et al., 2003) but the structure of the lithosphere may only be defined at a local scale, as large portions remain inaccessible. Differently, seismic data are endowed with a more continuous spatial coverage, to such an extent that the mantle may be imaged at a lithospheric scale; however, their conversion into models of the upper mantle is not straightforward (Afonso et al., 2013, and references therein). The interpretation of seismic data relies on appropriate combinations of the observed seismic wave velocities with either thermodynamic concepts and/or experimental data from mineral physics (e.g., Bass and Anderson, 1984) and needs to account for both compositional and thermal signatures in wave velocities. Uncertainties in data interpretation are further exacerbated since ultramafic rocks with different compositions can fit equally well wave velocities (e.g., Afonso et al., 2013).

In general, addressing the thermochemical structure of the mantle requires the calculation of mineral and rock physical properties (elastic *moduli*, thermal expansions, densities, etc.) at elevated pressure and temperature. Unequivocally, the knowledge of accurate elastic parameters of candidate mantle phases, and their variations with pressure and temperature, is required. In this context, the Equations of State (EoS) of mantle phases are undoubtedly the best proxy for unravelling the structure and dynamics of the Earth's mantle (e.g., Afonso et al., 2007; Stixrude and Lithgow-Bertelloni, 2005a) and its evolution through time, as they can define how volume, density or the elastic properties of minerals vary with pressure and/or temperature (e.g., Angel, 2000). For rocks, the elastic properties have to be inferred from those of their constituent minerals, at appropriate conditions (Connolly, 2009). This is commonly done by phase equilibria calculations based on thermodynamic data (Afonso et al., 2008; Connolly and Petrini, 2002; Stixrude and Lithgow-Bertelloni, 2005b; Stixrude and Lithgow-Bertelloni, 2011) (see Connolly, 2009 for extensive considerations of phase equilibria calculations to geodynamic modelling), with aggregate properties calculated by any standard solid mixing theory (e.g., Abers and Hacker, 2016; Hacker and Abers, 2004, and references therein). As mass in aggregates is a simple sum of chemical component masses, the density of rocks can be then calculated from the density of constituent minerals according to their volume proportion.

Several studies attempted to evaluate the density distribution of the lithosphere, known to be vertically and laterally heterogeneous due to variable mineralogy (in terms of mineral and modal compositions), complex phase transitions and differing thermal regimes. It was showed that the increase of Mg/(Mg + Fe) during partial melting lowers the bulk density of the mantle (Schutt and Lesher, 2006), but is not affecting phase transitions unlike Na content, which controls the spinel – plagioclase transition and may play an important role in areas of high heat flows and thin crust (Simon and Podladchikov, 2008). Further studies investigated the density structure of mantle sections either by combining data from petrology, mineral physics and geophysics (e.g., Fullea et al., 2014) or by classic thermodynamic calculations complemented for the most relevant Cr-bearing phases in the upper mantle (Ziberna and Klemme, 2016). These studies showed some contrasting results as to whether the predominant control on the density variations of the lithosphere is due to the thermal state, bulk composition, or their interplay.

In this work, we set out to explore the density structure of the lithospheric mantle, and its variation with changes in bulk composition and thermal gradient, from the perspective of the EoS of its constituent minerals, following a simplified parameterisation. The first part presents an assessment of the thermoelastic parameters of orthopyroxene, clinopyroxene, spinel and garnet. To this aim, pre-existing literature data on compressibility, thermal expansion and elasticity of these phases were used to constrain their P–V–T–K (P = pressure, V = volume, T = temperature, K = bulk modulus) EoS in peridotitic systems (i.e., preferentially selecting data measured on crystals with chemical compositions comparable to those expected in the upper mantle). As already computed in recent detailed studies, P–V–T–K and P–V–T EoS for mantle olivine and magnesiochromite were selected from literature (Angel et al., 2018; Nestola et al., 2019); two distinct EoS were used for mantle spinels to account for the variation of their elastic properties in response to varying Cr and Al contents (cfr. Section 2.3). The second part of this work aims at investigating how the density structure of fertile and depleted lithospheric mantle sections is affected by different thermal regimes (35, 45 and 60 mWm^{-2} geothermal gradients), following a simplified parameterisation that does not incorporate phase relations. Beyond exploring the density variations with this approach, we also provide a comparison with classic thermodynamic modelling (Perple_X; Ziberna and Klemme, 2016). This comparison allowed to assess that (i) the density profiles can be readily computed following our simplified parameterisation, (ii) the thermal gradient is the controlling variable when it comes to the density structure of the lithosphere and (iii) the newly developed and selected EoS consistently describe the elastic behaviour of the related phases under the most relevant P–T conditions and compositions of the Earth's mantle, without requiring sets of end-member properties and solution models.

2. Data selection and EoS fitting

There are two possible approaches to describe the P–V–T or P–V–T–K behaviour of solids: thermal-pressure models (Holland-Powell and Mie-Grüneisen-Debye thermal-pressure EoS) and isothermal-type models at high temperature (cfr. Angel et al., 2018). For extensive considerations to these issues the reader is referred to Anderson (1995), Angel (2000) and Angel et al. (2018).

The thermoelastic properties for mantle olivine ($Fo_{90–92}$) have been extensively reviewed and the P–V–T–K EoS was recently published (Angel et al., 2018). Considering the P – T ranges of our investigation, we selected the third-order Birch-Murnaghan compressional EoS in combination with the isothermal-type model for all the computations.

The P–V–T EoS for mantle magnesiochromite was also recently published (Nestola et al., 2019), parametrised as second-order Birch-Murnaghan compressional EoS in combination with the Holland-Powell thermal-pressure EoS; this formulation was used for the computations of magnesiochromite for the depleted peridotitic system. The selected thermoelastic parameters for mantle olivine and mantle magnesiochromite are reported in Table 1.

The thermoelastic behaviour of pyroxenes, spinel and garnet was here constrained based on X-Ray diffraction data (compressibility and thermal expansion) and elasticity measurements available in literature. The full EoS for these phases were solved with the EosFit7c program (Angel et al., 2014) following the approach of Milani et al. (2017) to perform simultaneous fits of elastic moduli and cell parameters. For every phase, each individual data set of volumes was scaled to its own volume at room conditions prior to fitting the data together. Additionally, in order to compare X-Ray diffraction and elasticity measurements, K_{SR} (adiabatic Reuss bulk moduli, from elasticity data) were converted into K_{TR} (isothermal Reuss bulk moduli, from X-Ray diffraction data) according to the relationship $K_{SR} = (1 + \alpha_V \gamma T) K_{TR}$ where α_V is the volume thermal expansion (taken from the EoS itself, at the P – T of interest) and γ is the Grüneisen parameter (taken from literature).

Table 1
Thermoelastic parameters selected from literature ([1] Angel et al., 2018; [2] Nestola et al., 2019) and derived from the fitting of P–V–T–K data for mantle phases. BM3 – Isothermal = Third-order Birch-Murnaghan compressional EoS in combination with the isothermal-type model (parameterisation from Angel et al., 2018); BM3 – HP = Third-order Birch-Murnaghan compressional EoS in combination with the Holland-Powell thermal-pressure EoS; BM2 – HP = Second-order Birch-Murnaghan compressional EoS in combination with the Holland-Powell thermal-pressure EoS.

	Olivine [1] BM3 – Isothermal	Orthopyroxene BM3 – Isothermal	Clinopyroxene BM3 – Isothermal	Spinel BM3 – HP	Magnesiochromite [2] BM2 – HP	Garnet BM3 – HP
$K_{TR,0}$ (GPa)	126.4(2)	111.8(7)	112.8(3)	194.8(2)	183.3(5)	168.63(20)
$K'_{TR,0}$	4.51(5)	7.39(19)	4.95(9)	4.64(7)	4 *fixed*	5.11(9)
$K''_{TR,0}$	−0.0368 *implied*	−0.1681 *implied*	−0.0509 *implied*	−0.0254 *implied*	−0.0212 *implied*	−0.0369 *implied*
α_{V0} (K^{-1})	2.666(9) x 10^{-5}	2.591(18) x 10^{-5}	2.67(7) x 10^{-5}	1.86(2) x 10^{-5}	1.66(2) x 10^{-5}	2.392(9) x 10^{-5}
θ_E (K)	484(6)	510 *fixed*	343(58)	714(15)	683(16)	450(6)
δ_T	5.77(7)	9.0(6)	4.84(17)	–	–	–
δ'	−3.5(1.1)	0 *fixed*	0 *fixed*	–	–	–
γ_0	1.044 *fixed*	0.85 *fixed*	0.867 *fixed*	1.17 *fixed*	–	1.19 *fixed*
q	1.88 *fixed*	0 *fixed*	0 *fixed*	0 *fixed*	–	0 *fixed*
χ^2	*not reported*	0.94	0.44	0.93	1.1	1.51
N data	121	73	74	93	53	85

2.1. Orthopyroxene

Mantle orthopyroxenes (space group *Pbca*) are solid solutions between enstatite ($Mg_2Si_2O_6$) and ferrosilite ($Fe_2Si_2O_6$) end-members and typically contain few wt% of Al_2O_3 and some CaO as well (e.g., McDonough and Rudnick, 1998). A reanalysis of K_{TR} and its pressure derivative K'_{TR} of $Mg_2Si_2O_6$ based on different experiments (two compression, one Brillouin measurement and one ultrasonic measurement) (Angel and Jackson, 2002) yielded the best estimates of $K_{TR,0}$ and $K'_{TR,0}$, being respectively 105.8(5) GPa and 8.5(3). By comparison, measurements on aluminium-bearing natural orthopyroxenes showed higher bulk moduli and lower pressure derivatives (Chai et al., 1997; Hugh-Jones et al., 1997; Zhang and Bass, 2016, refit of their data) than that of $Mg_2Si_2O_6$. For these reasons, $Mg_2Si_2O_6$ enstatite cannot be considered a good representation of the elastic behaviour of the orthopyroxene component in the lithospheric upper mantle.

We selected data from five different experiments on mantle orthopyroxenes: two compressions (Hugh-Jones and Angel, 1997) [samples *N1* and *N2*]), two expansions (Yang and Ghose, 1994 [sample *Fs20*]; Scandolo et al., 2015 [sample *B22 N.60*]) and one high-pressure Brillouin measurement (Zhang and Bass, 2016). We are not aware of any volume measurements on either mantle-composition orthopyroxene or enstatite made at low temperature; consequently, the Einstein temperature (θ_E) could not be refined and was fixed at 510 K (Holland and Powell, 2011, corresponding to Fs20). The Grüneisen parameter (0.85, for Fs20) was taken from Yang and Ghose (1994) and assumed that it does not vary with temperature. With these constraints, we fitted simultaneously each individual data set with a third-order Birch-Murnaghan compressional EoS in combination with the isothermal-type model (parameterisation from Angel et al., 2018); the final refined EoS parameters (Table 1) fit all the data within the experimental uncertainties (Supplementary Material File 1, Fig. S1). The final EoS for mantle orthopyroxene is provided in Supplementary Material File 2.

2.2. Clinopyroxene

Mantle clinopyroxenes (space group *C2/c*) are solid solutions between diopside ($CaMgSi_2O_6$) and hedenbergite ($CaFeSi_2O_6$) end-members and typically contain few wt% of Al_2O_3, some Cr_2O_3 as well as Na_2O (e.g., McDonough and Rudnick, 1998).

A survey of the literature showed that $K_{TR,0}$ and $K'_{TR,0}$ values for $CaMgSi_2O_6$ diopside and near end-member compositions exhibit large variations; the same is for $K_{S,0}$ and $K'_{S,0}$ (see Xu et al., 2019 for a recent compilation of literature data).

We selected data from six different experiments on diopside and near end-member compositions: one compression (Li and Neuville, 2010 [room temperature data]), three expansions (Cameron et al., 1973 [sample *Diopside*]; Pandolfo et al., 2015 [sample *Di*]; Prencipe et al., 2000), one high-pressure Brillouin measurement (Sang and Bass, 2014) and one high-temperature RUS measurement (Isaak et al., 2006). The Grüneisen parameter (0.867) is taken from Isaak et al. (2006) and assumed that it does not vary with temperature. $K_{SR,0}$ for near end-member diopsides recalculated from C_{ij} data of Sang and Bass (2014) and Isaak et al. (2006) are significantly different between each other (respectively, 111.2(7) GPa vs 113.4(9) GPa). To make the fit consistent between these two data sets, we excluded $K_{SR,0}$ of Sang and Bass (2014). We also excluded from the fit the data point of Sang and Bass (2014) at 14 GPa, which lies completely outside the trend (Supplementary Material File 1, Fig. S2). With these constraints, we fitted simultaneously each individual data set with a third-order Birch-Murnaghan compressional EoS in combination with the isothermal-type model (parameterisation from Angel et al., 2018); the final refined EoS parameters (Table 1) fit almost all the data within the experimental uncertainties (Supplementary Material File 1, Fig. S2). The final EoS for mantle clinopyroxene is provided in Supplementary Material File 3.

Bearing in mind that the selected data sets correspond to near end-member and $CaMgSi_2O_6$ diopside, it must be considered carefully whether the final refined thermoelastic parameters are a good representation of the elastic behaviour of the clinopyroxene component in the lithospheric upper mantle. Indeed, clinopyroxenes with augitic compositions are a common species occurring in a wide variety of igneous rocks and can be occasionally found in ultrabasic rocks. Xu et al. (2017) and (2019) recently studied the thermoelastic behaviour of augite by synchrotron-based X-Ray diffraction combined with an externally heated diamond anvil cell. Their experiments yielded respectively $K_{TR,0}$ = 111(1) GPa, $K'_{TR,0}$ = 4.1(1) and $K_{TR,0}$ = 112(3) GPa, $K'_{TR,0}$ = 5.0(7). These results prove that clinopyroxenes with augitic compositions behave similarly to near end-member diopsides. Therefore, we are confident that our P–V–T–K EoS parameters can be applied to a wide range of mantle clinopyroxene compositions.

2.3. Spinel

Mantle spinels (space group *Fd-3m*) show extensive solid solution between end-members as they typically vary in composition between four components: spinel s.s. ($MgAl_2O_4$), hercynite ($FeAl_2O_4$), magnesiochromite ($MgCr_2O_4$) and chromite ($FeCr_2O_4$). The compositional variations in mantle spinels are mainly displayed in their Cr/(Cr + Al) and Mg/(Mg + Fe) molar ratios, which reflect the degree of melt depletion experienced by a peridotite. Indeed, spinels with high Al and low Cr contents characterize lherzolites, whereas low Al and high Cr contents distinguish harzburgitic spinels (e.g., McDonough and Rudnick, 1998).

The bulk modulus systematics for Mg-Fe-Cr-Al spinels have been recently analysed by Nestola et al. (2015, and references therein), who showed that: (i) the Cr-Al substitution considerably changes the $K_{TR,0}$

[192(1) vs 182.5(1.4) GPa for $MgAl_2O_4$ and $MgCr_2O_4$, respectively]; (ii) the Fe-Mg substitution does not substantially affect the bulk modulus for either Cr or Al spinels [193.9(1.7) vs 184.8(1.7) GPa for $FeAl_2O_4$ and $FeCr_2O_4$, respectively], with the $K'_{TR,0}$ similar for all four end-members. Thus, the $K_{TR,0}$ of Mg-Fe-Cr-Al spinels is roughly controlled by the Cr/Al ratio. Hence, two EoS are needed to properly describe the elastic behaviour of mantle spinels: one EoS for lherzolitic spinels and another EoS (selected from Nestola et al., 2019, see above) for harzburgitic spinels (magnesiochromites).

To constrain the elastic behaviour of Al-rich lherzolitic spinels, we selected data from six different experiments: one compression (Nestola et al., 2007 [sample *disordered*]), three expansions (Carbonin et al., 2002 [sample *NAT*]; Grimes and Al-Ajaj, 1992; Martignago et al., 2003 [sample *H-Cr*]), one high-pressure Brillouin measurement (Speziale et al., 2016) and one high-temperature RPR measurement (Suzuki et al., 2000). The Grüneisen parameter (1.17) was taken from Suzuki et al. (2000) and assumed that it does not vary with temperature. Because the quoted uncertainties of K_{SR} from Suzuki et al. (2000) are substantially smaller than those expected from elasticity measurements (e.g. 1 to 3 GPa), we under-weighted the experimental data (1% esd was assumed for all data). With these constraints, we fitted simultaneously each individual data set with a third-order Birch-Murnaghan compressional EoS in combination with the Holland-Powell thermal-pressure EoS; the final refined EoS parameters (Table 1) fit almost all the data within the experimental uncertainties (Supplementary Material File 1, Fig. S3). The final EoS for mantle spinel is provided in Supplementary Material File 4. Considering the bulk modulus systematics for Mg-Fe-Cr-Al spinels, we are confident that our P–V–T–K EoS parameters can be applied to a wide range of Al-rich spinel compositions.

2.4. Garnet

Mantle garnets (space group *Ia-3d*, general formula $X_3Y_2Si_3O_{12}$) are multicomponent substitutional solid solutions since different cations can be mutually exchanged at the X (Mg, Fe, Ca, Mn divalent cations) and Y (Al, Fe, Cr trivalent cations) sites. Compositionally, the most significant components of peridotitic garnets are $Mg_3Al_2Si_3O_{12}$ pyrope (ca 75%), $Ca_3Al_2Si_3O_{12}$ grossular (ca 10%) and $Fe_3Al_2Si_3O_{12}$ almandine (ca 15%) (e.g., Wood et al., 2013).

The effect of Mg-Fe substitution for the pyrope-almandine solid solution was recently analysed by Lu et al. (2013) and Milani et al. (2015). Milani et al. (2015) determined $K_{TR,0} = 163.7(1.7)$ GPa for pyrope, $K_{TR,0} = 167.2(1.7)$ GPa for an intermediate $Py_{60}Alm_{40}$ and $K_{TR,0} = 172.6(1.5)$ GPa for almandine, with similar $K'_{TR,0}$ for all three garnets, claiming that Fe substituting for Mg linearly increases $K_{TR,0}$ but does not affect $K'_{TR,0}$. However, compared to the sources reviewed by Milani et al. (2015), the determined $K_{TR,0}$ values are notably lower than expected whereas $K'_{TR,0}$ are slightly higher and this can be ascribed to the well-known trade-off between fit values for $K_{TR,0}$ and $K'_{TR,0}$. Lu et al. (2013) measured the elasticity of a Fe-bearing pyrope by high P-T Brillouin spectroscopy, determining $K_{SR,0} = 168.2(1.8)$ and $K'_{SR,0} = 4.4(1)$. Comparative analysis of these results led the authors to conclude that addition of Fe does significantly affect $K_{SR,0}$ but rather has a weak positive effect on $K'_{SR,0}$. A similar conclusion was reached by Jiang et al. (2004), who showed that Fe substituting for Mg in the pyrope-almandine series has a little effect on the bulk modulus (almandine $K_{SR,0}$ being 2% higher than that of pyrope) while it increases its pressure derivative. The effect of Ca-Mg substitution for the pyrope-grossular solid solution has been analysed again by Jiang et al. (2004), who showed that the $K_{SR,0}$ varies by ca 2% across the pyrope-grossular system and that there are no evident trends in the $K'_{SR,0}$. In view of these considerations, we selected data from four different experiments: one compression (Milani et al., 2015 [sample $Py_{60}Alm_{40}$]), two expansions (Bosenick and Geiger, 1997 [excluding the scattered data at 220 K], Milani et al., 2015 [sample Py_{100}]) and one high-temperature RUS measurement (Suzuki and Anderson, 1983). The Grüneisen parameter (1.19) was taken from Gillet et al. (1992) and assumed that it does not vary with temperature. With these constraints, we fitted simultaneously each individual data set with a third-order Birch-Murnaghan compressional EoS in combination with the Holland-Powell thermal-pressure EoS; the final refined EoS parameters (Table 1) fit all the data within the experimental uncertainties (Supplementary Material File 1, Fig. S4). The final EoS for mantle garnet is provided in Supplementary Material File 5. Considering the bulk modulus systematics for Mg-Fe-Ca aluminous garnets, we are confident that our P–V–T–K EoS parameters can be applied to a wide range of mantle garnet compositions.

3. Density variations in the lithospheric mantle

3.1. Density calculations

The density of mantle peridotites is function of the chemical composition, modal abundance and elastic properties of their constituent minerals, which in turn are controlled by pressure, temperature and bulk composition of the system. Here, the density structure of the lithospheric mantle was calculated following a two-step approach.

The first step involved the calculation of density profiles for each phase along the geothermal gradients of interest. To our purposes, three geothermal gradients of 35, 45 and 60 mWm^{-2} were chosen as considered representative of extremely cold, intermediate, and relatively hot lithospheric sections. The density of each phase was calculated in the form of 'crystallographic density' according to the relation:

$$\rho_{(phase\ at\ PT)} = \frac{Z_{(phase)} \times Mw_{(phase)}}{\left(\frac{V}{V0}\right)_{(EoS\ at\ PT)} \times V0_{(phase)} \times Na} \quad (1)$$

where $\left(\frac{V}{V0}\right)_{(EoS\ at\ PT)}$ represents the volume [here the normalized volume $\left(\frac{V}{V0}\right)$] calculated from the EoS at specific P – T conditions (e.g., for a characteristic geotherm or at any P – T), $V0_{(phase)}$ is the reference unit cell volume of the phase measured at ambient conditions, $Mw_{(phase)}$ its molecular weight, $Z_{(phase)}$ is the number of formula units in the unit cell and *Na* the Avogadro number.

The second step involved the calculation of density profiles for bulk rocks, which were here calculated from the densities ρ_i of n constituent minerals as:

$$\rho_{(bulk\ rock)} = \left(\sum_{i=1}^{n} \rho_i \times v_i\right) \Big/ n \quad (2)$$

where v_i is the volume proportion of each mineral.

We computed density profiles for all constituent mineral phases and for two potential lithospheric mantle sections, a fertile and a depleted peridotitic systems, along the 35, 45 and 60 mWm^{-2} geothermal gradients. Calculations for the two lithospheric sections were restricted to a P – T range of 1–8 GPa and 350–1375 °C. These gradients were selected from the preferred geotherm family of Hasterok and Chapman (2011), which are based on radiogenic heat production measurements together with xenolith thermobarometry and tectonothermal constraints. Following Hasterok and Chapman (2011), we assumed that the transition from a conductive to an adiabatic geotherm corresponds to the lithosphere-asthenosphere boundary (LAB), which is here used only to discuss the effect of temperature on density profiles.

Our calculations at subsolidus conditions do not include the effects of porosity, mineral texture and rock microstructure as well as no volatile-bearing phases, thus excluding OH groups in NAMs and/or intergranular fluids and/or melts.

Calculations were based on previously studied natural peridotite xenoliths: a spinel lherzolite from the Veneto Volcanic Province (sample SG34 from Beccaluva et al., 2001) was adopted as representative of a

fertile mantle, while a spinel harzburgite from Grande Comore island (sample NDR13, unpublished data from Coltorti et al., 1999), now under investigation for other petrological studies, was chosen to represent a depleted mantle. Modal compositions of the selected samples were calculated by least-squares mass balance using bulk-rock and mineral major element analyses (Tables 2, 3).

Bearing in mind that calculating the density of each phase requires a reference unit cell volume measured at ambient conditions ($V0_{(phase)}$, eq. 1), olivine, pyroxenes, spinel and garnet unit cell parameters (and related crystal chemical compositions, which slightly differ compared to those expected from our models of fertile and depleted mantle) were selected from literature (Tables 2, 3). Modal compositions were kept from the two selected mantle xenoliths (SG34 spinel lherzolite and NDR13 spinel harzburgite), however density calculations were carried out by using the mineral compositions and unit cell volumes of the reference minerals from the literature. All selected mineral compositions were kept fixed for all density calculations.

The spinel-garnet transition was modelled according to the approximate reaction spinel + pyroxenes = garnet + olivine (e.g., Klemme and O'Neill, 2000); mineral modes in the garnet stability field were calculated from stoichiometric balance upon completion of the reaction (Tables 2, 3). Recent thermodynamic modelling in natural peridotitic systems (Ziberna et al., 2013) indicates that garnet and spinel always coexist and the width and depth of the coexistence interval strongly, but not only, depends on the thermal state of the lithosphere (restricted depth interval - about 15 km - in regions with hot geotherms, and much broader interval - over 100 km - for cold geotherms). We simplified this model by assuming garnet + spinel coexistence intervals of 1.5–4 GPa, 1.5–3 GPa and 1.8–2.4 GPa along the 35, 45 and 60 mWm^{-2} geothermal gradients, respectively, for both fertile and depleted mantle sections. For density calculations, mineral modes were kept fixed in spinel and garnet stability fields, and were imposed to vary linearly in the spinel-garnet stability field.

3.2. Results

Density profiles for both mineral phases and the fertile and depleted peridotitic systems were calculated along three different geothermal gradients: 35 mWm^{-2} (Figs. 1, 2), representative of the coldest cratonic mantle sections, 45 mWm^{-2} (Figs. 1, 3), typical of average cratonic sections, and 60 mWm^{-2} (Figs. 1, 4), for relatively hot, off-craton, lithospheric sections (Hasterok and Chapman, 2011).

Fig. 1 shows that, despite mineral phases having different elastic parameters (Table 1), their density variation with depth is largely controlled by the geothermal gradients. Under cold conditions (35 mWm^{-2}), density curves for all phases shows a subtle but significant decrease down to ca 1 GPa, which is followed by a marked increase for olivine and pyroxenes and a moderate increase for spinel, magnesiochromite and garnet. Under relatively hot conditions (60 mWm^{-2}), density curves for all phases exhibit a marked decrease down to ca 3 GPa, followed by an increase with depth. It is under intermediate conditions (45 mWm^{-2}) and at $P > 1$ GPa that density curves exhibit most of the differences. Indeed, density curves for all mineral phases show a gentle decrease down to ca 1 GPa, where the density of olivine and pyroxenes starts to increase, whereas it continues to decrease down to ca 4.5 GPa for spinel, magnesiochromite and garnet. Such distinct behaviour is clearly due to different elastic parameters (Table 1), but it is also due to the interplay between increasing temperature and pressure, whose effects are of the same order (see also considerations below). Noteworthy errors associated with density calculations through the newly developed and two selected EoS are minimum (Fig. 1), and this in turn affects the accuracy of density profiles for bulk rocks. Such errors, esd($\rho/\rho 0$) $\sim 10^{-3}$, translate to uncertainties of density calculations which are $\sim$ 0.05% (e.g., 3.416(2) g/cm^3 or conversely 3416(2) kg/m^3 at $\sim$ 6 GPa and $\sim$1050 °C for the fertile peridotitic system), which are considerably much less than average uncertainties associated to density calculations.

If we consider a geotherm of 35 mWm^{-2} and both fertile and depleted compositions (Fig. 2), the density in the mantle shows a similar behaviour, progressively increasing with increasing depth. This indicates that the effect of pressure prevails over that of the slowly rising temperature. By comparing the trends of the fertile and depleted mantle sections (Fig. 5), it is evident that the former is typified by a more pronounced density increase with respect to the depleted one. This is attributable to the higher modes of garnet (due to higher bulk Al_2O_3 in fertile compositions), which is among the densest mineral phases in peridotite assemblages (e.g., Lee, 2003).

If we consider a geotherm of 45 mWm^{-2}, results are somehow different in the 1–4 GPa interval. Here, the density of the depleted peridotitic system remains nearly constant while it moderately increases for the fertile system; then the density of both systems increases from 4 down to 8 GPa (Figs. 3, 5). These results suggest that (i) the effect of temperature on the evolution of the bulk density with depth is comparable to that of pressure and that (ii) the behaviour of the two systems is decoupled down to ca 4 GPa.

If we consider a relatively hot geotherm of 60 mWm^{-2}, the temperature increase with depth is so strong that leads to an overall decrease of the bulk density of both depleted and fertile systems in the

Table 2
Mineral phases compositions (a.p.f.u.) and modes (SG34 spinel lherzolite) and selected reference phases for the computation of density profiles for the fertile lithospheric mantle section.

	Olivine		Orthopyroxene		Clinopyroxene		Spinel		Garnet	
	Model	Selected [1]	Model	Selected [2]	Model	Selected [3]	Model	Selected [4]	Model	Selected [5]
Si	0.9955	1.00	1.8690	1.89	1.8570	1.8756	n.d.	n.d.	n.a.	3.0005
Ti	n.d.	n.d.	0.0029	n.d.	0.0136	0.0129	0.0016	0.0031	n.a.	0.0272
Al	n.d.	n.d.	0.2225	0.23	0.3437	0.2833	1.7484	1.7673	n.a.	1.7749
Cr	n.d.	n.d.	0.0115	0.01	0.0256	0.0275	0.1734	0.1871	n.a.	0.1202
Fe*	0.2106	0.20	0.2046	0.17	0.0983	0.0907	0.2761	0.2237	n.a.	0.5317
Mn	0.0017	n.d.	0.0035	0.01	0.0031	0.0026	0.0020	0.0020	n.a.	0.0217
Mg	1.7882	1.80	1.6745	1.63	0.7705	0.8513	0.7915	0.8090	n.a.	2.1868
Ca	0.0005	n.d.	0.0201	0.04	0.7782	0.7596	n.d.	n.d.	n.a.	0.3326
Na	n.d.	n.d.	n.d.	n.d.	0.1097	0.1050	n.d.	n.d.	n.a.	n.d.
K	n.d.	n.d.	n.d.	n.d.	n.d.	n.d.	n.d.	n.d.	n.a.	n.d.
Ni	0.0079	n.d.	0.0025	n.d.	n.d.	0.0001	0.0070	0.0079	n.a.	n.d.
Zn	n.d.	n.d.	n.d.	n.d.	n.d.	n.d.	0.0035	n.d.	n.a.	n.d.
Unit cell volume [$Å^3$]	n.a.	292.01(10)	n.a.	834.1(5)[#]	n.a.	432.96(4)	n.a.	538.78(6)	–	1535.2(5)[#]
Mode [spl stability field]	61.8		20.0		16.6		1.6		0.0	
Mode [grt stability field]	64.4		15.1		14.8		0.0		5.7	

References: [1] Zha et al., 1998; [2] Chai et al., 1997, [3] Brown and Collins, 1998; [4] Ono et al., 2018; [5] Sumino and Nishizawa, 1978 (PY-1 sample); [#] = esd assumed, Fe* = total iron, n.d. = not detected, n.a. = not available.

Table 3
Mineral phases compositions (a.p.f.u.) and modes (NDR13 spinel harzburgite) and selected reference phases for the computation of density profiles for the depleted lithospheric mantle section.

	Olivine		Orthopyroxene		Clinopyroxene		Magnesiochromite		Garnet	
	Model	Selected [1]	Model	Selected [2]	Model	Selected [3]	Model	Selected [4]	Model	Selected [5]
Si	1.0031	1.00	1.9687	1.968	1.9568	1.962	0.0004	n.d.	n.a.	3.0105
Ti	n.d.	n.d.	0.0005	n.d.	0.0021	0.002	0.0017	n.d.	n.a.	0.0160
Al	0.0004	n.d.	0.0545	0.037	0.0753	0.121	0.7961	1.00	n.a.	1.7297
Cr	0.0005	n.d.	0.0142	0.011	0.0494	0.023	1.1240	0.92	n.a.	0.1780
Fe*	0.1851	0.20	0.1682	0.146	0.0816	0.072	0.3618	0.31	n.a.	0.4874
Mn	0.0028	n.d.	0.0044	n.d.	0.0029	0.001	0.0019	n.d.	n.a.	0.0198
Mg	1.7965	1.80	1.7454	1.813	0.9779	0.890	0.7057	0.77	n.a.	2.1910
Ca	0.0012	n.d.	0.0344	0.025	0.7985	0.828	0.0003	n.d.	n.a.	0.3575
Na	n.d.	n.d.	0.0071	n.d.	0.0642	0.102	n.d.	n.d.	n.a.	n.d.
K	n.d.	n.d.	n.d.	n.d.	0.0004	n.d	n.d.	n.d.	n.a.	n.d.
Ni	0.0070	n.d.	0.0025	n.d.	0.0019	n.d	0.0045	n.d.	n.a.	n.d.
Zn	n.d.	n.d.	n.d.	n.d.	n.d.	n.d	0.0035	n.d.	n.a.	n.d.
Unit cell volume [Å^3]	n.a.	292.01(10)	n.a.	834.71(3)	n.a.	434.42(48)	n.a.	560.68(16)	–	1537.20(46)
Mode [spl stability field]		85.4		12.0		1.6		1.0		0.0
Mode [grt stability field]		86.7		9.3		0.9		0.0		3.1

References: [1] Zha et al., 1998; [2] Gatta et al., 2007; [3] Comodi et al., 1995 (sample 3211); [4] Matsukage et al., 2010; [5] Babuška et al., 1978 (PY-2 sample); Fe* = total iron, n.d. = not detected, n.a. = not available.

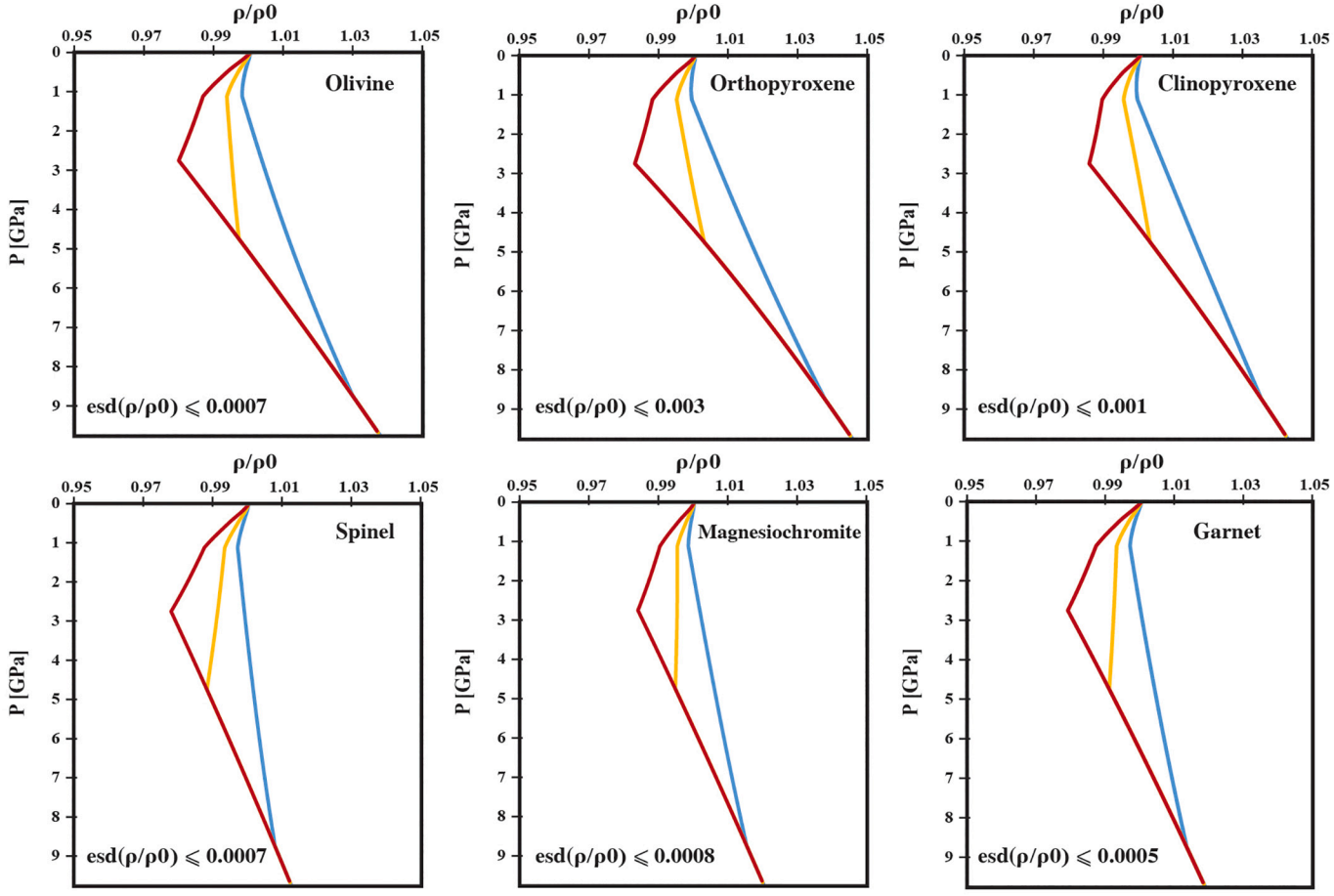

Fig. 1. Density profiles (ρ/ρ0) for mineral phases in the studied peridotitic systems (olivine, orthopyroxene, clinopyroxene, spinel, magnesiochromite and garnet) calculated along a 35 mWm^{-2} geotherm (blue curves), 45 mWm^{-2} geotherm (yellow curves) and 60 mWm^{-2} geotherm (red curves). The 35, 45 and 60 mWm^{-2} conductive geotherms for density calculations are from Hasterok and Chapman (2011). Esd(ρ/ρ0) (estimated standard deviation) refers to the uncertainties associated with EoS fitting (as calculated by the least-squares method) and density calculations. Note that these uncertainties are minimum. (For interpretation of the references to colour in this figure legend, the reader is referred to the web version of this article.)

lithosphere from 1 to about 3 GPa, followed by an increase from 3 down to 8 GPa (Fig. 4). By comparing the trends of the two sections (Fig. 5), the fertile system shows a more gentle decrease in its density compared to the depleted system. This is again attributable to the higher modes of garnet, which, combined with the P – T gradient effects, result in a slightly smoother density profile. Irrespective of the specific depth and width of their coexistence intervals, spinel and garnet have a stronger control on the density variations in case of fertile compositions, due to

their higher modes.

3.3. Discussion

3.3.1. Density models and the effect of the thermal state

Most of the recently published upper mantle density models derive from phase equilibria calculations based on thermodynamic data, where stable mineral assemblages are computed using Gibbs free-energy minimization techniques. Previous works (Fullea et al., 2014; Ziberna and Klemme, 2016) showed some contrasting results as to whether the lithospheric density is predominantly controlled by the thermal state, bulk composition, or their interplay. Fullea et al. (2014) unravelled the present-day Irish lithospheric structure through LitMod3D code (Fullea et al., 2009) that combines petrological and geophysical observations with thermodynamic data (in the CFMAS system) within a self-consistent framework. This modelling revealed similar vertical density profiles - sharp spinel – garnet phase transition with an abrupt increase of density, a general trend of decreasing density down to ~ 100 km, followed by an increase (Fig. 5) - associated with all the mantle compositions discussed in the work (i.e., from fertile to moderately depleted peridotites). Overall, these density trends suggest a greater control of the thermal state on the lithospheric density rather than bulk composition in the Irish lithosphere (60 to 70 mWm^{-2}). Considering the lack of Cr (for which there is evidence that it may considerably change phase relations in the upper mantle) in most previous calculations, Ziberna and Klemme (2016) investigated the density variations for Cr-bearing mantle compositions (Pali-Aike xenoliths, Patagonia) in response to changes in bulk compositions and thermal gradients by means of well-established free energy minimization techniques, with thermodynamic calculations based on the internally consistent dataset of Holland and Powell (1998) complemented for the most relevant Cr-bearing phases in the upper mantle (Ziberna et al., 2013). Contrary to previous results (Fullea et al., 2014), this work showed that the density profiles across the spinel – garnet peridotite transition are not sharp and depend both on bulk composition (especially on Al_2O_3 and Cr_2O_3) and geothermal gradient (Fig. 5). Moreover, while under relatively hot thermal conditions (70 mWm^{-2}) density profiles for both fertile and depleted compositions show similar trends (i.e., density decrease down to ca 2.5 GPa), this is not the case for intermediate thermal conditions (50 mWm^{-2}) where density in the mantle for depleted compositions remains virtually constant down to ca 4 GPa and it rapidly increases for more fertile compositions (Fig. 5). Accordingly, these authors suggested that it is the interplay between bulk composition and thermal gradient that controls density variations in the lithospheric mantle.

Our models predict a much greater thermal control over the density of the lithospheric mantle, with some compositional control mostly arising at cold-intermediate thermal conditions (Fig. 5). Considering that we based the spinel – garnet phase transitions on Ziberna et al. (2013) thermodynamic model (cfr. Section 3.1), spinel and garnet coexist over a significant depth interval. Accordingly, our models predict a smooth variation of densities across the spinel – garnet transition and no abrupt changes. As already evidenced by Ziberna and Klemme (2016), the sharp spinel – garnet transitions associated with an abrupt change of density identified by Fullea et al. (2014) can be ascribed to the lack of Cr in their thermodynamic model. If this aspect is ruled out from further discussion, and density curves are analysed overall, there are some similarities with those from Fullea et al. (2014) (Fig. 5). Indeed, all modelled compositions exhibit an overall decrease of the bulk density up to about 100 km, followed by an increase downwards, for relatively hot thermal conditions (60 to 70 mWm^{-2}). Our density curves show even more striking similarities with those from Ziberna and Klemme (2016), for which a similar behaviour is predicted for fertile and depleted compositions under relatively hot thermal conditions (70 mWm^{-2}), and a different one under intermediate conditions (50 mWm^{-2}) (Fig. 5). Therefore, our investigation shows that density profiles in natural systems with simplified phase relations display comparable trends to those reported in previous studies. In this framework, perspectives are that the thermal gradient exerts substantial control when it comes to the density structure of the lithosphere and that the compositional control on the density evolution with depth may be less than previously suggested. In the next section, we show how density calculations based on simplified phase relations can be reconciled with Perple_X-based results from

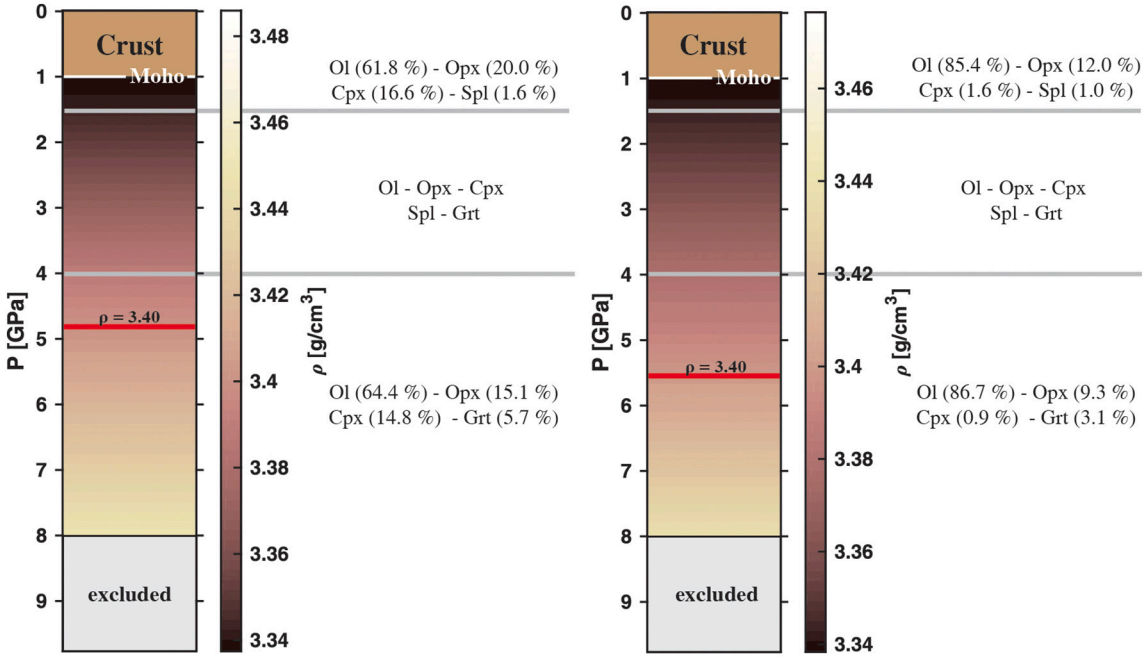

Fig. 2. Density profiles for fertile (left panel) and depleted (right panel) peridotitic systems calculated along a 35 mWm^{-2} geotherm. Brown to yellow colour bar represents the density variations along the profiles. Grey lines subdivide the ideal mantle sections into the spinel, spinel + garnet and garnet stability fields, following a simplification of Ziberna et al. (2013) thermodynamic model. The isodensity line for $\rho = 3.40$ g/cm^3 is shown for reference. (For interpretation of the references to colour in this figure legend, the reader is referred to the web version of this article.)

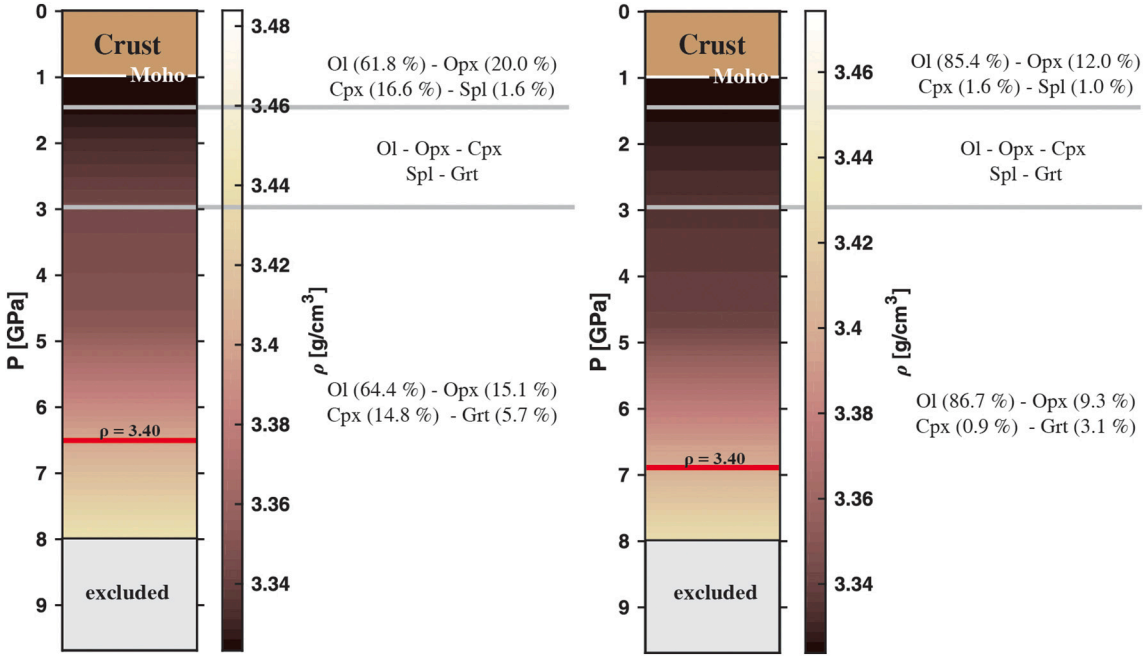

Fig. 3. Density profiles for fertile (left panel) and depleted (right panel) peridotitic systems calculated along a 45 mWm^{-2} geotherm. Brown to yellow colour bar represents the density variations along the profiles. Grey lines subdivide the ideal mantle sections into the spinel, spinel + garnet and garnet stability fields, following a simplification of Ziberna et al. (2013) thermodynamic model. The isodensity line for $\rho = 3.40$ g/cm^3 is shown for reference. (For interpretation of the references to colour in this figure legend, the reader is referred to the web version of this article.)

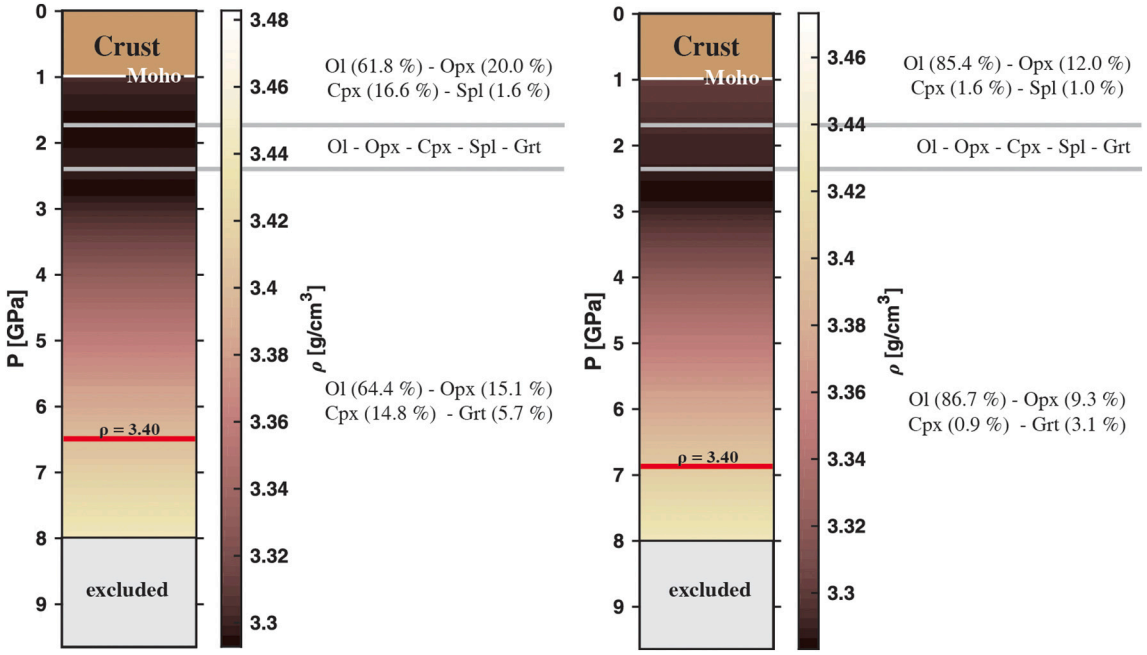

Fig. 4. Density profiles for fertile (left panel) and depleted (right panel) peridotitic systems calculated along a 60 mWm^{-2} geotherm. Brown to yellow colour bar represents the density variations along the profiles. Grey lines subdivide the ideal mantle sections into the spinel, spinel + garnet and garnet stability fields, following a simplification of Ziberna et al. (2013) thermodynamic model. The isodensity line for $\rho = 3.40$ g/cm^3 is shown for reference. (For interpretation of the references to colour in this figure legend, the reader is referred to the web version of this article.)

previous literature. We also infer the thermal gradient is the main controlling variable of the lithospheric mantle density.

3.3.2. *Comparison between Perple_X and simplified calculations*

Although a strict evaluation of similarities and differences of our simplified parameterisation for calculating density variations with respect to classic thermodynamic modelling (e.g., Perple_X) goes beyond the scope of this paper (detailed results of the application of both models to a real mantle section will be presented elsewhere), in the following we provide an application of our model compared with previous results from literature (Ziberna and Klemme, 2016). To this aim, we selected two of the four representative mantle xenoliths from Pali-Aike, Patagonia, reported in Ziberna and Klemme (2016), namely PA3 (spinel harzburgite) and BN4 (spinel-garnet lherzolite), for which we computed

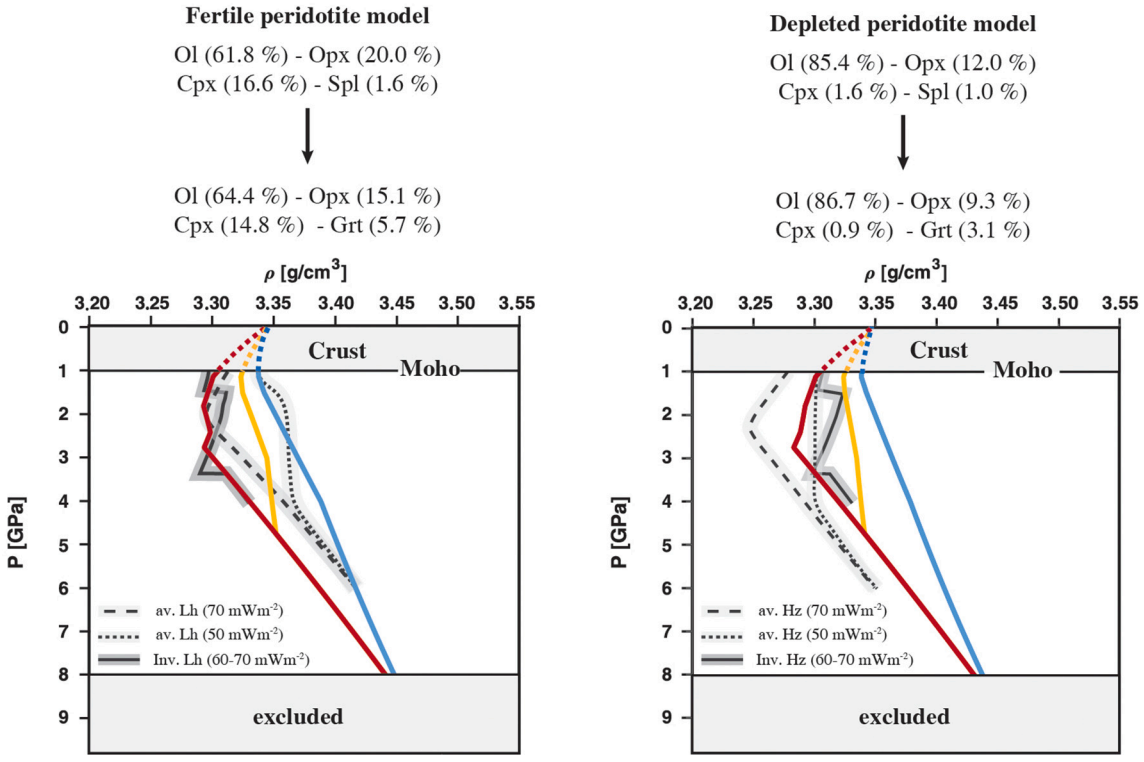

Fig. 5. Comparison of density profiles for fertile (left panel) and depleted (right panel) peridotitic systems calculated along a 35 mWm^{-2} geotherm (blue curves), 45 mWm^{-2} geotherm (yellow curves) and 60 mWm^{-2} geotherm (red curves). Density curves from previous literature are also shown: av. Lh (70 mWm^{-2}), av. Lh (50 mWm^{-2}), av. Hz (70 mWm^{-2}) and av. Hz (50 mWm^{-2}) are respectively the average density curves for fertile (TM16, BN4) and depleted (LS1, PA3) mantle xenoliths from Ziberna and Klemme (2016) calculated along the 70 mWm^{-2} and 50 mWm^{-2} geothermal gradients, whereas Inv. Lh (60–70 mWm^{-2}) and Inv. Hz (60–70 mWm^{-2}) are respectively the density curves of Inver lherzolite and harzburgite mantle xenoliths from Fullea et al. (2014) calculated under the Irish thermal state (60 to 70 mWm^{-2}). (For interpretation of the references to colour in this figure legend, the reader is referred to the web version of this article.)

density profiles along the 50 and 70 mWm^{-2} geothermal gradients (Fig. 6). Input data for Ziberna and Klemme (2016) thermodynamic modelling are whole-rock analyses from Stern et al. (1999), with calculations performed in the SiO_2-Al_2O_3-Cr_2O_3-FeO-MgO-CaO-Na_2O system. In order to provide a clear and consistent comparison between the two methods, input data (i.e., mineral compositions and modes) for our simplified parameterisation were as follows. Olivine, pyroxenes, and spinel mineral compositions and modes were selected from Perple_X calculations of Ziberna and Klemme (2016) at 1 GPa (at the corresponding temperature for the 50 and 70 mWm^{-2} geothermal gradients). Garnet compositions were selected from Perple_X calculations of Ziberna and Klemme (2016) at P – T corresponding to spinel-out

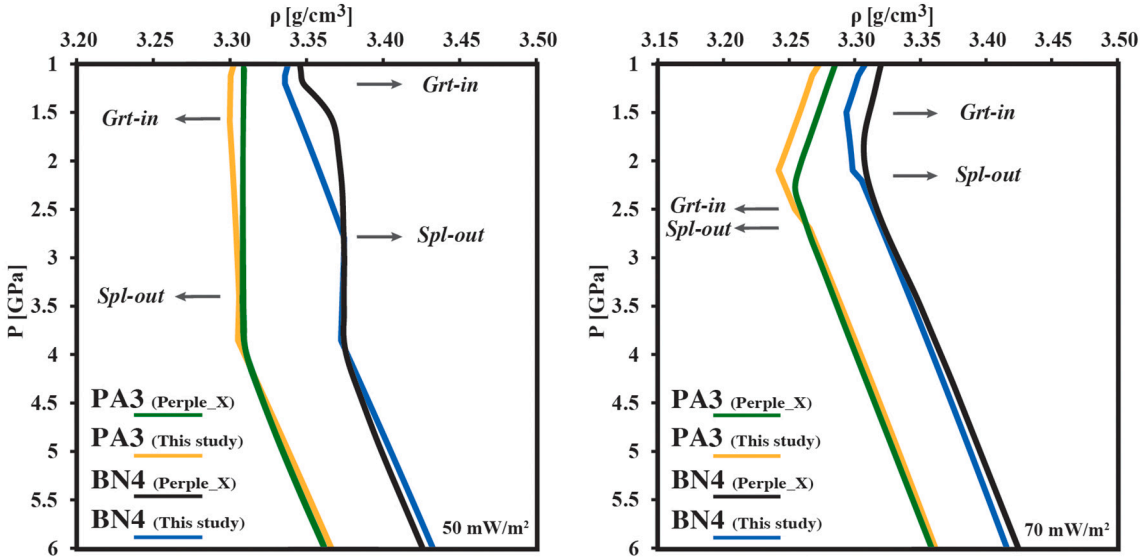

Fig. 6. Density profiles for PA3 (spinel harzburgite) and BN4 (spinel-garnet lherzolite) mantle xenoliths calculated along the 50 and 70 mWm^{-2} geothermal gradients following our simplified parameterisation in comparison with Perple_X-based original curves from Ziberna and Klemme (2016). Note the similarities between the two distinct sets of curves, both in their general trends and absolute values, as the density difference is always <20 kg/m^3.

reaction (which depends on bulk composition and geothermal gradient); garnet, as well as olivine and pyroxenes modes in the garnet stability field, were calculated from stoichiometric balance upon completion of the reaction spinel + pyroxenes = garnet + olivine, using the selected mineral modes and compositions. Selected mineral compositions were kept fixed along the whole section; mineral modes were kept fixed in spinel and garnet stability fields, and were imposed to vary linearly in the spinel-garnet stability field (cfr. Section 3.1). Depth intervals of coexistence of spinel + garnet were selected again from Perple_X calculations of Ziberna and Klemme (2016). Density variations with depth and thermal regime for PA3 (spinel harzburgite) and BN4 (spinel-garnet lherzolite) mantle xenoliths are reported in Fig. 6, along with original curves from Ziberna and Klemme (2016).

Note that Ziberna and Klemme (2016) thermodynamic model considered phase equilibria, with mineral modes and compositions continuously changing according to P – T conditions, which has not been done in this study. Nonetheless, density curves calculated with our simplified parameterisation match well those from Ziberna and Klemme (2016), both in their general trends with depth and absolute values, with a maximum difference between the two models of ca 20 kg/m^3 (Fig. 6). From this similarity, we conclude that our approach with simplified phase relations has enough accuracy for investigating the density structure of the lithosphere. We also infer that the density structure of the lithospheric mantle is predominantly controlled by the thermal gradient variations, with most of the compositional control arising at cold-intermediate thermal conditions. No less importantly, we showed that the newly developed P–V–T–K EoS (pyroxenes, spinel and garnet) in combination with the published EoS for mantle olivine and mantle magnesiochromite are applicable for calculating the density of mantle peridotites and its variation, with minimum uncertainties, under different thermal regimes and bulk compositions, without requiring sets of end-member properties and solution models.

4. Concluding remarks

In this study, we presented an assessment of the thermoelastic parameters of orthopyroxene, clinopyroxene, spinel and garnet based on X-Ray diffraction data and direct elastic measurements available in literature. The newly developed EoS consistently describe the elastic behaviour of these phases under the most relevant P–T conditions and bulk compositions of the Earth's mantle, along with the published EoS for mantle olivine and magnesiochromite.

As a case study, we evaluated the influence of bulk composition and thermal regimes on the density structure of potential lithospheric mantle sections, following a simplified parameterisation that does not incorporate phase relations. Accordingly, density profiles for fertile and depleted peridotitic systems based on the EoS of their constituent mineral phases were calculated for three different geothermal gradients (35, 45 and 60 mWm^{-2}), for a P – T range of 1–8 GPa and 350–1375 °C. In case of very cold geotherms (35 mWm^{-2}), the density of both depleted and fertile systems progressively increases with increasing depth. In case of intermediate geotherms (45 mWm^{-2}), the density of a depleted peridotitic system remains nearly constant up to about 4 GPa, while it moderately increases in a fertile system, due to higher modes of garnet. In case of relatively hot geotherms (60 mWm^{-2}), the density of both depleted and fertile systems progressively decreases with increasing depth, up to about 3 GPa, and then increases downwards. Moreover, we also provided an example of application of our model in comparison with classic thermodynamic modelling results from literature. From such comparison, we concluded that (i) density profiles for mantle sections can be computed with enough accuracy following our simplified parameterisation, (ii) the thermal gradient exerts substantial control when it comes to the density structure of the lithosphere and (iii) the compositional control on the density evolution with depth may be less than previously suggested.

Funding

L.F. acknowledges Istituto Nazionale di Geofisica e Vulcanologia (INGV) for funding his Ph.D. project (XXXV cycle) with thematic 'Links between rheology, mineralogy and composition of the Earth's mantle' and the Italian National Research Program (PRIN Grant 20178LPCPW 'Micro to Macro - How to unravel the nature of the Large Magmatic Events' to [M.C.])

Declaration of Competing Interest

The authors declare that they have no known competing financial interests or personal relationships that could have appeared to influence the work reported in this paper.

Acknowledgements

Dr. Luca Ziberna is thanked for providing work files that allowed a validation of our simplified parameterisation for calculating density variations with respect to Perple_X models. The authors are grateful to Michel Grégoire and an anonymous reviewer for their constructive comments, which improved an earlier version of the manuscript. Michael Roden is acknowledged for his careful editorial handling and guidance.

Appendix A. Supplementary data

Supplementary data to this article can be found online at https://doi.org/10.1016/j.lithos.2021.106483.

References

Abers, G.A., Hacker, B.R., 2016. A MATLAB toolbox and Excel workbook for calculating the densities, seismic wave speeds, and major element composition of minerals and rocks at pressure and temperature. Geochem. Geophys. Geosyst. 17, 616–624. https://doi.org/10.1002/2015GC006171.

Afonso, J.C., Ranalli, G., Fernàndez, M., 2007. Density structure and buoyancy of the oceanic lithosphere revisited. Geophys. Res. Lett. 34, 2–6. https://doi.org/10.1029/2007GL029515.

Afonso, J.C., Fernàndez, M., Ranalli, G., Griffin, W.L., Connolly, J.A.D., 2008. Integrated geophysical-petrological modeling of the lithosphere and sublithospheric upper mantle: Methodology and applications. Geochem. Geophys. Geosyst. 9 https://doi.org/10.1029/2007GC001834. Q05008.

Afonso, J.C., Fullea, J., Yang, Y., Connolly, J.A.D., Jones, A.G., 2013. 3-D multi-observable probabilistic inversion for the compositional and thermal structure of the lithosphere and upper mantle. II: General methodology and resolution analysis. J. Geophys. Res. Solid Earth 118, 1650–1676. https://doi.org/10.1002/jgrb.50123.

Anderson, O.L., 1995. Equations of state of solids for geophysics and ceramic science. Oxf. Monogr. Geol. Geophys. https://doi.org/10.1016/0016-7037(95)90195-7.

Angel, R.J., 2000. Equations of State. Rev. Mineral. Geochem. 41, 35–59. https://doi.org/10.2138/rmg.2000.41.2.

Angel, R.J., Jackson, J.M., 2002. Elasticity and equation of state of orthoenstatite, MgSiO 3. Am. Mineral. 87, 558–561. https://doi.org/10.2138/am-2002-0419.

Angel, R.J., Alvaro, M., Gonzalez-Platas, J., 2014. EosFit7c and a Fortran module (library) for equation of state calculations. Zeitschrift für Krist. - Cryst. Mater. 229, 405–419. https://doi.org/10.1515/zkri-2013-1711.

Angel, R.J., Alvaro, M., Nestola, F., 2018. 40 years of mineral elasticity: a critical review and a new parameterisation of equations of state for mantle olivines and diamond inclusions. Phys. Chem. Miner. 45, 95–113. https://doi.org/10.1007/s00269-017-0900-7.

Babuška, V., Fiala, J., Kumazawa, M., Ohno, I., Sumino, Y., 1978. Elastic properties of garnet solid-solution series. Phys. Earth Planet. Inter. 16, 157–176. https://doi.org/10.1016/0031-9201(78)90086–9.

Bass, J.D., Anderson, D.L., 1984. Composition of the upper mantle: Geophysical tests of two petrological models. Geophys. Res. Lett. 11, 229–232. https://doi.org/10.1029/GL011i003p00229.

Beccaluva, L., Bonadiman, C., Coltorti, M., Salvini, L., Siena, F., 2001. Depletion events, nature of metasomatizing agent and timing of enrichment processes in lithospheric mantle xenoliths from the Veneto Volcanic Province. J. Petrol. 42, 173–188. https://doi.org/10.1093/petrology/42.1.173.

Bosenick, A., Geiger, C.A., 1997. Powder X ray diffraction study of synthetic pyrope-grossular garnets between 20 and 295 K. J. Geophys. Res. Solid Earth 102, 22649–22657. https://doi.org/10.1029/97JB01612.

Braun, J., 2010. The many surface expressions of mantle dynamics. Nat. Geosci. 3, 825–833. https://doi.org/10.1038/ngeo1020.

Brown, J.M., Collins, M.D., 1998. Elasticity of an upper mantle clinopyroxene. Phys. Chem. Miner. 26, 7–13. https://doi.org/10.1007/s002690050156.
Cameron, M., Sueno, S., Prewitt, C.T., Papike, J.J., 1973. High-Temperature crystal chemistry of acmite, diopside, hedenbergite, jadeite, spodumene, and Ureyite. Am. Mineral. 58, 594–618.
Capitanio, F., Morra, G., Goes, S., 2007. Dynamic models of downgoing plate-buoyancy driven subduction: Subduction motions and energy dissipation. Earth Planet. Sci. Lett. 262, 284–297. https://doi.org/10.1016/j.epsl.2007.07.039.
Carbonin, S., Martignago, F., Menegazzo, G., Dal Negro, A., 2002. X-ray single-crystal study of spinels: in situ heating. Phys. Chem. Miner. 29, 503–514. https://doi.org/10.1007/s00269-002-0262-6.
Chai, M., Brown, J.M., Slutsky, L.J., 1997. The elastic constants of an aluminous orthopyroxene to 12.5 GPa. J. Geophys. Res. Solid Earth 102, 14779–14785. https://doi.org/10.1029/97JB00893.
Coltorti, M., Bonadiman, C., Hinton, R.W., Siena, F., Upton, B.G.J., 1999. Carbonatite metasomatism of the oceanic upper mantle: evidence from clinopyroxenes and glasses in ultramafic xenoliths of grande comore, Indian Ocean. J. Petrol. 40, 133–165. https://doi.org/10.1093/petroj/40.1.133.
Coltorti, M., Bonadiman, C., Casetta, F., Faccini, B., Giacomoni, P.P., Pelorosso, B., Perinelli, C., 2021. Nature and evolution of the northern Victoria Land lithospheric mantle (Antarctica) as revealed by ultramafic xenoliths. Geol. Soc. Lond. Mem. 56 https://doi.org/10.1144/M56-2020-11. M56–2020–11.
Comodi, P., Princivalle, F., Tirone, M., Zanazzi, P.F., 1995. Comparative compressibility of clinopyroxenes from mantle nodules. Eur. J. Mineral. 7, 141–150. https://doi.org/10.1127/ejm/7/1/0141.
Connolly, J.A.D., 2009. The geodynamic equation of state: What and how. Geochem. Geophys. Geosyst. 10, Q10014. https://doi.org/10.1029/2009GC002540.
Connolly, J.A.D., Petrini, K., 2002. An automated strategy for calculation of phase diagram sections and retrieval of rock properties as a function of physical conditions. J. Metamorph. Geol. 20, 697–708. https://doi.org/10.1046/j.1525-1314.2002.00398.x.
Fullea, J., Afonso, J.C., Connolly, J.A.D., Fernàndez, M., García-Castellanos, D., Zeyen, H., 2009. LitMod3D: An interactive 3-D software to model the thermal, compositional, density, seismological, and rheological structure of the lithosphere and sublithospheric upper mantle. Geochem. Geophys. Geosyst. 10 https://doi.org/10.1029/2009GC002391.
Fullea, J., Muller, M.R., Jones, A.G., Afonso, J.C., 2014. The lithosphere–asthenosphere system beneath Ireland from integrated geophysical–petrological modeling II: 3D thermal and compositional structure. Lithos 189, 49–64. https://doi.org/10.1016/j.lithos.2013.09.014.
Gatta, G.D., Rinaldi, R., Knight, K.S., Molin, G., Artioli, G., 2007. High temperature structural and thermoelastic behaviour of mantle orthopyroxene: an in situ neutron powder diffraction study. Phys. Chem. Miner. 34, 185–200. https://doi.org/10.1007/s00269-006-0138-2.
Gillet, P., Fiquetw, G., Malézieux, J.M., Geiger, C.A., 1992. High-pressure and high-temperature Raman spectroscopy of end-member garnets: pyrope, grossular and andradite. Eur. J. Mineral. 4, 651–664. https://doi.org/10.1127/ejm/4/4/0651.
Grimes, N.W., Al-Ajaj, E.A., 1992. Low-temperature thermal expansion of spinel. J. Phys. Condens. Matter 4, 6375–6380. https://doi.org/10.1088/0953-8984/4/30/004.
Hacker, B.R., Abers, G.A., 2004. Subduction Factory 3: An Excel worksheet and macro for calculating the densities, seismic wave speeds, and H 2 O contents of minerals and rocks at pressure and temperature. Geochem. Geophys. Geosyst. 5 https://doi.org/10.1029/2003GC000614 n/a-n/a.
Hasterok, D., Chapman, D.S., 2011. Heat production and geotherms for the continental lithosphere. Earth Planet. Sci. Lett. 307, 59–70. https://doi.org/10.1016/j.epsl.2011.04.034.
Holland, T.J.B., Powell, R., 1998. An internally consistent thermodynamic data set for phases of petrological interest. J. Metamorph. Geol. 16, 309–343. https://doi.org/10.1111/j.1525-1314.1998.00140.x.
Holland, T.J.B., Powell, R., 2011. An improved and extended internally consistent thermodynamic dataset for phases of petrological interest, involving a new equation of state for solids. J. Metamorph. Geol. 29, 333–383. https://doi.org/10.1111/j.1525-1314.2010.00923.x.
Hugh-Jones, D.A., Angel, R.J., 1997. Effect of Ca 2+ and Fe 2+ on the equation of state of MgSiO 3 orthopyroxene. J. Geophys. Res. Solid Earth 102, 12333–12340. https://doi.org/10.1029/96JB03485.
Hugh-Jones, D., Chopelas, A., Augel, R., 1997. Tetrahedral compression in (Mg,Fe)SiO 3 orthopyroxenes. Phys. Chem. Miner. 24, 301–310. https://doi.org/10.1007/s002690050042.
Isaak, D.G., Ohno, I., Lee, P.C., 2006. The elastic constants of monoclinic single-crystal chrome-diopside to 1,300 K. Phys. Chem. Miner. 32, 691–699. https://doi.org/10.1007/s00269-005-0047-9.
Jiang, F., Speziale, S., Duffy, T.S., 2004. Single-crystal elasticity of grossular- and almandine-rich garnets to 11 GPa by Brillouin scattering. J. Geophys. Res. Solid Earth 109, 1–10. https://doi.org/10.1029/2004JB003081.
Klemme, S., O'Neill, H.S., 2000. The near-solidus transition from garnet lherzolite to spinel lherzolite. Contrib. Mineral. Petrol. 138, 237–248. https://doi.org/10.1007/s004100050560.
Lee, C.-T.A., 2003. Compositional variation of density and seismic velocities in natural peridotites at STP conditions: Implications for seismic imaging of compositional heterogeneities in the upper mantle. J. Geophys. Res. Solid Earth 108, 2441. https://doi.org/10.1029/2003JB002413.
Li, B., Neuville, D.R., 2010. Elasticity of diopside to 8GPa and 1073K and implications for the upper mantle. Phys. Earth Planet. Inter. 183, 398–403. https://doi.org/10.1016/j.pepi.2010.08.009.
Lu, C., Mao, Z., Lin, J.-F., Zhuravlev, K.K., Tkachev, S.N., Prakapenka, V.B., 2013. Elasticity of single-crystal iron-bearing pyrope up to 20GPa and 750K. Earth Planet. Sci. Lett. 361, 134–142. https://doi.org/10.1016/j.epsl.2012.11.041.
Martignago, F., Negro, A.D., Carbonin, S., 2003. How Cr3+ and Fe3+ affect Mg?Al order?Disorder transformation at high temperature in natural spinels. Phys. Chem. Miner. 30, 401–408. https://doi.org/10.1007/s00269-003-0336-0.
Mazzucchelli, M., Rivalenti, G., Brunelli, D., Zanetti, A., Boari, E., 2009. Formation of highly refractory dunite by focused percolation of pyroxenite-derived melt in the Balmuccia Peridotite Massif (Italy). J. Petrol. 50, 1205–1233. https://doi.org/10.1093/petrology/egn053.
Matsukage, K.N., Kikuchi, S., Ono, S., Nishihara, Y., Kikegawa, T., 2010. Density and seismic velocities of chromitite body in oceanic mantle peridotite. Am. Mineral. 95, 1422–1428. https://doi.org/10.2138/am.2010.3498.
McDonough, W.F., Rudnick, R.L., 1998. Mineralogy and composition of the upper mantle. Rev. Mineral. 37, 139–164.
Melchiorre, M., Faccini, B., Grégoire, M., Benoit, M., Casetta, F., Coltorti, M., 2020. Melting and metasomatism/refertilisation processes in the Patagonian sub-continental lithospheric mantle: a review. Lithos 354–355, 105324. https://doi.org/10.1016/j.lithos.2019.105324.
Milani, S., Nestola, F., Alvaro, M., Pasqual, D., Mazzucchelli, M.L., Domeneghetti, M.C., Geiger, C.A., 2015. Diamond–garnet geobarometry: the role of garnet compressibility and expansivity. Lithos 227, 140–147. https://doi.org/10.1016/j.lithos.2015.03.017.
Milani, S., Angel, R.J., Scandolo, L., Mazzucchelli, M.L., Ballaran, T.B., Klemme, S., Domeneghetti, M.C., Miletich, R., Scheidl, K.S., Derzsi, M., Tokár, K., Prencipe, M., Alvaro, M., Nestola, F., 2017. Thermo-elastic behavior of grossular garnet at high pressures and temperatures. Am. Mineral. 102, 851–859. https://doi.org/10.2138/am-2017-5855.
Nestola, F., Ballaran, T.B., Balic-Zunic, T., Princivalle, F., Secco, L., Dal Negro, A., 2007. Comparative compressibility and structural behavior of spinel MgAl2O4 at high pressures: the independency on the degree of cation order. Am. Mineral. 92, 1838–1843. https://doi.org/10.2138/am.2007.2573.
Nestola, F., Periotto, B., Anzolini, C., Andreozzi, G.B., Woodland, A.B., Lenaz, D., Alvaro, M., Princivalle, F., 2015. Equation of state of hercynite, FeAl2O4, and high-pressure systematics of Mg-Fe-Cr-Al spinels. Mineral. Mag. 79, 285–294. https://doi.org/10.1180/minmag.2015.079.2.07.
Nestola, F., Zaffiro, G., Mazzucchelli, M.L., Nimis, P., Andreozzi, G.B., Periotto, B., Princivalle, F., Lenaz, D., Secco, L., Pasqualetto, L., Logvinova, A.M., Sobolev, N.V., Lorenzetti, A., Harris, J.W., 2019. Diamond-inclusion system recording old deep lithosphere conditions at Udachnaya (Siberia). Sci. Rep. 9, 12586. https://doi.org/10.1038/s41598-019-48778-x.
Ono, K., Harada, Y., Yoneda, A., Yamamoto, J., Yoshiasa, A., Sugiyama, K., Arima, H., Watanabe, T., 2018. Determination of elastic constants of single-crystal chromian spinel by resonant ultrasound spectroscopy and implications for fluid inclusion geobarometry. Phys. Chem. Miner. 45, 237–247. https://doi.org/10.1007/s00269-017-0912-3.
Pandolfo, F., Cámara, F., Domeneghetti, M.C., Alvaro, M., Nestola, F., Karato, S.-I., Amulele, G., 2015. Volume thermal expansion along the jadeite–diopside join. Phys. Chem. Miner. 42, 1–14. https://doi.org/10.1007/s00269-014-0694-9.
Pearson, D.G., Canil, D., Shirey, S.B., 2003. Mantle samples included in volcanic rocks: xenoliths and diamonds. In: Treatise on Geochemistry. Elsevier, pp. 171–275. https://doi.org/10.1016/B0-08-043751-6/02005–3.
Prencipe, M., Tribaudino, M., Pavese, A., Hoser, A., Reehuis, M., 2000. A single-crystal neutron-diffraction investigation of diopside at 10 k. Can. Mineral. 38, 183–189. https://doi.org/10.2113/gscanmin.38.1.183.
Sang, L., Bass, J.D., 2014. Single-crystal elasticity of diopside to 14GPa by Brillouin scattering. Phys. Earth Planet. Inter. 228, 75–79. https://doi.org/10.1016/j.pepi.2013.12.011.
Scandolo, L., Mazzucchelli, M.L., Alvaro, M., Nestola, F., Pandolfo, F., Domeneghetti, M.C., 2015. Thermal expansion behaviour of orthopyroxenes: the role of the Fe-Mn substitution. Mineral. Mag. 79, 71–87. https://doi.org/10.1180/minmag.2015.079.1.07.
Schutt, D.L., Lesher, C.E., 2006. Effects of melt depletion on the density and seismic velocity of garnet and spinel lherzolite. J. Geophys. Res. Solid Earth 111. https://doi.org/10.1029/2003JB002950.
Simon, N.S.C., Podladchikov, Y.Y., 2008. The effect of mantle composition on density in the extending lithosphere. Earth Planet. Sci. Lett. 272, 148–157. https://doi.org/10.1016/j.epsl.2008.04.027.
Speziale, S., Nestola, F., Jiang, F., Duffy, T.S., 2016. Single-crystal elastic constants of spinel (MgAl2O4) to 11.1 GPa by Brillouin scattering. In: AGU Fall Meeting Abstracts (pp. MR23A-2658).
Stern, C.R., Kilian, R., Olker, B., Hauri, E.H., Kurtis Kyser, T., 1999. Evidence from mantle xenoliths for relatively thin (<100 km) continental lithosphere below the Phanerozoic crust of southernmost South America. Lithos 48, 217–235. https://doi.org/10.1016/S0419-0254(99)80013-5.
Stixrude, L., Lithgow-Bertelloni, C., 2005a. Mineralogy and elasticity of the oceanic upper mantle: Origin of the low-velocity zone. J. Geophys. Res. 110, B03204 https://doi.org/10.1029/2004JB002965.
Stixrude, L., Lithgow-Bertelloni, C., 2005b. Thermodynamics of mantle minerals - I. Physical properties. Geophys. J. Int. 162, 610–632. https://doi.org/10.1111/j.1365-246X.2005.02642.x.
Stixrude, L., Lithgow-Bertelloni, C., 2011. Thermodynamics of mantle minerals - II. Phase equilibria. Geophys. J. Int. 184, 1180–1213. https://doi.org/10.1111/j.1365-246X.2010.04890.x.

Sumino, Y., Nishizawa, O., 1978. Temperature variation of elastic constants of pyrope-almandine garnets. J. Phys. Earth 26, 239–252. https://doi.org/10.4294/jpe1952.26.239.

Suzuki, I., Anderson, O.L., 1983. Elasticity and thermal expansion of a natural garnet up to 1,000K. J. Phys. Earth 31, 125–138. https://doi.org/10.4294/jpe1952.31.125.

Suzuki, I., Ohno, I., Anderson, O.L., 2000. Harmonic and anharmonic properties of spinel MgAl 2 O 4. Am. Mineral. 85, 304–311. https://doi.org/10.2138/am-2000-2-307.

Thybo, H., Artemieva, I.M., 2013. Moho and magmatic underplating in continental lithosphere. Tectonophysics 609, 605–619. https://doi.org/10.1016/j.tecto.2013.05.032.

Wood, B.J., Kiseeva, E.S., Matzen, A.K., 2013. Garnet in the Earth's Mantle. Elements 9, 421–426. https://doi.org/10.2113/gselements.9.6.421.

Xu, J., Zhang, D., Dera, P., Zhang, B., Fan, D., 2017. Experimental evidence for the survival of augite to transition zone depths, and implications for subduction zone dynamics. Am. Mineral. 102, 1516–1524. https://doi.org/10.2138/am-2017-5959.

Xu, Z., Ma, M., Li, B., Hong, X., 2019. Compressibility and thermal expansion of natural clinopyroxene Di0.66Hd0.13Jd0.12Ts0.05. Results Phys. 12, 447–453. https://doi.org/10.1016/j.rinp.2018.11.077.

Yang, H., Ghose, S., 1994. Thermal expansion, Debye temperature and Gruneisen parameter of synthetic (Fe, Mg)SiO3 orthopyroxenes. Phys. Chem. Miner. 20, 575–586. https://doi.org/10.1007/BF00211853.

Zha, C., Duffy, T.S., Downs, R.T., Mao, H., Hemley, R.J., 1998. Brillouin scattering and X-ray diffraction of San Carlos olivine: direct pressure determination to 32 GPa. Earth Planet. Sci. Lett. 159, 25–33. https://doi.org/10.1016/S0012-821X(98)00063–6.

Zhang, J.S., Bass, J.D., 2016. Single-crystal elasticity of natural Fe-bearing orthoenstatite across a high-pressure phase transition. Geophys. Res. Lett. 43, 8473–8481. https://doi.org/10.1002/2016GL069963.

Ziberna, L., Klemme, S., 2016. Application of thermodynamic modelling to natural mantle xenoliths: examples of density variations and pressure–temperature evolution of the lithospheric mantle. Contrib. Mineral. Petrol. 171, 16. https://doi.org/10.1007/s00410-016-1229-9.

Ziberna, L., Klemme, S., Nimis, P., 2013. Garnet and spinel in fertile and depleted mantle: insights from thermodynamic modelling. Contrib. Mineral. Petrol. 166, 411–421. https://doi.org/10.1007/s00410-013-0882-5.